

Continuum subtracting Lyman-alpha images: Low redshift studies using the Solar Blind Channel of HST/ACS

Matthew Hayes

matthew.hayes@unige.ch

Geneva Observatory, University of Geneva, 51 chemin des Maillettes, 1290 Sauverny, Switzerland

Göran Östlin¹

ostlin@astro.su.se

Stockholm Observatory, AlbaNova University Centre, SE-106 91 Stockholm, Sweden

J. Miguel Mas-Hesse²

Centro de Astrobiología (CSIC-INTA), E28850 Torrejon de Ardoz, Madrid, Spain

mm@laeff.inta.es

Daniel Kunth

Institut d'Astrophysique de Paris, Paris (IAP), 98 bis boulevard Arago, 75014 Paris, France

kunth@iap.fr

ABSTRACT

We are undertaking an imaging study of local star-forming galaxies in the Lyman-alpha ($\text{Ly}\alpha$) emission line using the *Solar Blind Channel (SBC)* of the *Advanced Camera for Surveys* onboard the *Hubble Space Telescope*. Observations have been obtained in $\text{Ly}\alpha$ and H-alpha ($\text{H}\alpha$) and six line-free continuum filters between $\sim 1500\text{\AA}$ and the *I*-band. In a previous article (Hayes et al. 2005) we demonstrated that the production of $\text{Ly}\alpha$ line-only images (i.e. continuum subtraction) in the *SBC*-only data-set is non-trivial and that supporting data is a requirement. We here develop various methods of continuum subtraction and assess their relative performance using a variety of spectral energy distributions (SED) as input. We conclude that simple assumptions about the behavior of the ultraviolet continuum consistently lead to results that are wildly erroneous, and determine that a spectral fitting approach is essential. Moreover, fitting of a single component stellar or stellar+nebular spectrum is not always sufficient for realistic template SEDs and, in order to successfully recover the input observables, care must be taken to control the contribution of nebular gas and any underlying stellar population. Independent measurements of the metallicity must first be obtained, while details of the initial mass function play only a small role. We identify the need to bin together pixels in our data to obtain signal-to-noise (S/N) ratios of around 10 in each band before processing. At $S/N = 10$ we are able to recover $\text{Ly}\alpha$ fluxes accurate to within around 30% for $\text{Ly}\alpha$ lines with intrinsic equivalent width

¹Oscar Klein Centre for Cosmoparticle physics, Department of Astronomy, Stockholm University, Sweden.

²Laboratorio de Astrofísica Espacial y Física Fundamental (LAEFF-INTA), POB 78, Vva. Canada, Spain

($W_{\text{Ly}\alpha}$) of 10\AA . This accuracy improves to $\lesssim 10\%$ for $W_{\text{Ly}\alpha}=100\text{\AA}$. We describe the method of image processing applied to the observations presented in Östlin et al. (2009) and the associated data-release. We also present simulations for an observing strategy for an alternative low-redshift Ly α imaging campaign using *ACS/SBC* using adjacent combinations of long-pass filters to target slightly higher redshift.

Subject headings: methods: data analysis — techniques: image processing — techniques: photometric — galaxies: starburst

1. Introduction

The Lyman-alpha emission line (Ly α) is a powerful and frequently exploited observational signature through which the galaxy population can be probed at high-redshift (z). In principle Ly α can be used to probe the ionization fraction during the final stages of re-ionization (Malhotra & Rhoads 2004; Dijkstra et al. 2007), cosmic star-formation rates (Hu et al. 1998; Kudritzki et al. 2000; Ajiki et al. 2003), large scale structure (Venemans et al. 2002; Ouchi et al. 2005), and to identify potential host of population III star formation (Malhotra & Rhoads 2002; Nagao et al. 2007). Ultimately, exactly how the Ly α -emitting (or non-emitting) high- z galaxy population relates to the ultraviolet-selected Lyman break galaxy (LBG) population is uncertain, and studies of the high- z population of Ly α emitters (LAEs) are interesting in their own right.

In all surveys for which the ultimate science goal is more fundamental than the observed population itself, it is vital to understand what biases, be they observational or astrophysical, may affect the inferred properties and how they manifest themselves. This point is especially consequential for high- z Ly α -selected studies where typical detections are faint and galaxies often go undetected in the continuum. Ly α is a resonant line and its formation is strongly affected by a complex radiative transport. On a physical level the regulation and transport of Ly α is known to be affected by dust, the topology and ionization of the ISM, HI kinematics, and viewing geometry. Such insights have been gleaned empirically from spectroscopic observations of small samples of local galaxies (Giavalisco et al. 1996; Kunth et al. 1998; Mas-Hesse et al. 2003), flanked by a sophisticated theoretical and computational attack on the problem of Ly α escape physics (Neufeld 1990; Ahn 2004; Hansen & Oh 2006; Verhamme et al. 2006; Laursen & Sommer-Larsen 2007).

Since Ly α is a resonance line and can be expected to be substantially spatially decoupled from UV continuum radiation and other nebular lines, the picture yielded by UV-targeted spectroscopy is limited. Thus the imaging approach becomes an invaluable complement to the previous *IUE* and *HST* spectroscopic studies. Ly α imaging at $z \approx 0$ is technically possible with *HST* using the *Wide Field and Planetary Camera (WFPC2)* although the instrumental throughput at Ly α would make it very inefficient. A much more economical approach would be to use the UV-optimized channels of the *Space Telescope Imaging Spectrograph (STIS)* or *Advanced Camera for Surveys (ACS)* which both offer higher system efficiency and better defined and non red-leaking filters. In *HST* cycle 11 we began an imaging study to examine a handful of local star-forming galaxies in Ly α using *HST/ACS*. First results from this were presented in Kunth et al. (2003), although technical uncertainties about how to subtract the continuum prevented a deep analysis and Hayes et al. (2005) demonstrated the need for additional off-line observations to aid in the continuum subtraction. This additional data has since been obtained for the remainder of the sample and the entire dataset has now been processed. Ly α line-only images are being released to the community (Östlin et al. 2009). However, since the process of subtracting the continuum in this study is far from trivial and future imaging studies depend upon the methodology, this process was deemed to be worthy of an article in its own right. We here perform a series of tests of synthetic Ly α imaging observations of low- z targets using configurations available on *HST* and compare different approaches to subtracting the continuum.

The article is organized as follows: in Sect. 2 we explain the complications involved with Ly α observations and why conventional continuum subtraction techniques are not applicable to Ly α with

the current instrumentation; in Sect. 3 we describe the methodology and theoretical tests; in Sect. 4 we present the results and discuss their significance; in Sect. 5 we present simulations for a study targeting slightly higher redshift and discuss some possible augmentation to the method; and in Sect. 6 we make some concluding remarks.

2. Local Lyman-alpha imaging

2.1. Observing strategies

The *Solar Blind Channel (SBC)* of *HST/ACS* offers the *F122M* filter through which to observe restframe Ly α at $0 < z \lesssim 0.035$. This filter peaks at 1216Å and has a rectangular width (W_r) of 128.4Å although the pivotal wavelength (λ_p) at 1273.7Å is rather offset from the peak due to the red wing. Furthermore, with $W_r/\lambda_p \approx 0.1$, this filter cannot be considered narrow compared to optical narrowband filters. A number of long-pass filters are available through which to sample the continuum, the most appropriate for $z \approx 0$ being *F140LP* ($\lambda_p=1527\text{Å}$; $W_r=252.95\text{Å}$). This *F122M+F140LP* configuration is that used by our imaging campaign and is denoted configuration 1 in this article. Due to the very sharp cut-on on the blue side, and the red side being defined by the degrading sensitivity of the detector with wavelength, all the long-pass filters exhibit near identical shapes in the red wing. Adjacent long-pass filter combinations could therefore be appropriate for Ly α imaging of slightly more distant targets (e.g. *F125LP+F140LP* for $0.028 \lesssim z \lesssim 0.1$) and this combination is also examined here, denoted as configuration 2. Fig. 1 shows the bandpasses for both configurations.

2.2. Continuum subtraction methods

The art of continuum subtraction hinges entirely upon scaling of the stellar continuum sampled by an off-line filter to the bandpass of the filter that isolates the line. In the forthcoming discussion we make use of a quantity known as the *Continuum Throughput Normalization (CTN)* factor, first defined in Hayes et al. (2005). This is the dimensionless quantity that scales the raw count-rate in a continuum filter to that expected in the on-line filter, accounting for the filter transmission profiles, the instrument sensitivity, and the shape

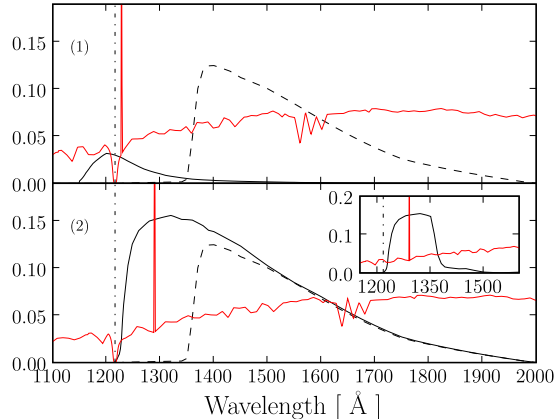


Fig. 1.— *ACS/SBC* filter combinations for Ly α imaging. Solid lines represent the filter that transmits Ly α and dashed lines that for the continuum. Vertical dot-dashed lines are at $\lambda = 1216\text{Å}$, the wavelength of both Milky Way Ly α absorption and the geocoronal emission line. The red line shows a synthetic spectrum with artificially added Ly α . For illustration, a Milky Way absorption feature has also been added to the templates ($\log(n_{\text{HI}}) = 20.5 \text{ cm}^{-2}$). *Upper*: Configuration 1: *F122M+F140LP* for $z \lesssim 0.03$. Suitable for $z \approx 0$ although both geocoronal emission and Galactic absorption fall in the on-line bandpass and must be accounted for. The spectrum is redshifted to 0.01. *Lower*: Configuration 2: *F125LP+F140LP* for $0.03 \lesssim z \lesssim 0.1$. Geocoronal Ly α is not transmitted and on-line system throughput is greatly improved over the *upper* example. The spectrum is redshifted to 0.06.

of the continuum. That is,

$$\text{Ly}\alpha = \text{online} - CTN \times \text{offline} \quad (1)$$

CTN can be computed with varying degrees of complexity. For known or assumed continuum slopes it can be computed simply from the inverse sensitivity bandpass characteristics (PHOT-FLAM) of the on- and off-line filters. For any continuum spectrum, CTN can be computed by convolving the spectrum with the instrument throughput profiles of the filters, integrating to estimate the count-rate, and calculating the ratio. This permits features such as spectral shape and absorption or emission lines to be accounted for in the process. In essence CTN is simply a color with a non-standard normalization derived from instrument sensitivities.

There are a number of possible issues that may impede the continuum subtraction of $\text{Ly}\alpha$. Firstly, possible strong stellar $\text{Ly}\alpha$ absorption may cancel some or all of the nebular emission. This is perhaps unlikely to be a strong affect where the starburst is very young and dominated by O-stars where deep absorption features have yet to develop. The effect may become very significant when $\text{Ly}\alpha$ is scattered and may be superimposed upon older stellar populations with lower effective temperature. Indeed, absorption of stellar continuum by B-stars was initially proposed as an explanation for the weakness or absence of $\text{Ly}\alpha$ emission in nearby starbursts and for the early failure to detect $\text{Ly}\alpha$ emitters at high- z (Valls-Gabaud 1993). Secondly, the $\text{Ly}\alpha$ feature may be P Cygni with some or all of the emission cancelled by absorption, especially directly in front of the brightest clusters. Spectroscopic measurements, if of sufficient resolution, can isolate the emission segment of the P Cygni profile and obtain the emitted flux, although this is not possible with imaging. If the absorption segment falls within the on-line filter as it will in our case, the local minima in $\text{Ly}\alpha$ flux from P Cygni absorption on top of clusters can never be corrected for. Notably however, this caveat also applies to imaging surveys at high- z . Ultimately what is called emission is a matter of definition; whether it be defined as the flux in the emission segment of the profile, or the flux integrated over both the absorption and emission segments. Either way, imaging can only assess the latter. Finally, and especially

for configuration 1, photometry will be directly affected by Milky Way $\text{Ly}\alpha$ absorption and geocoronal $\text{Ly}\alpha$ emission. Both of these effects can be relatively easily accounted for since they are not expected to vary strongly across the small angles subtended by the SBC field-of-view. Geocoronal emission can be removed by background subtraction, and Milky Way $\text{Ly}\alpha$ absorption computed from the HI column density measured along the line-of-sight to the target (Dickey & Lockman 1990; Kalberla et al. 2005) and incorporated into the calculation of CTN .

2.2.1. Purely observational methods

Typically, for optical emission lines in ground-based observations, continuum is sampled using a filter positioned as close as possible to, but not transmitting, the line in question (or other contaminating spectral features). For example, an off-line $\text{H}\alpha$ filter 100Å redward of the line corresponds to $\Delta\lambda/\lambda \sim 0.015$. Were an intrinsically power-law continuum with $\beta = -2$ assumed to be flat ($\beta = 0$), this would result in an error in the line-center continuum estimate of around 3%¹. Typically, this would be considered ‘good enough’.

The same is not true for the FUV filter set available on HST/SBC . Due to the limited choice of filters available, for the $F122M+F140LP$ the on- and off-line combination, the pivot wavelengths are separated by $\Delta\lambda/\lambda \sim 0.2$ which would result in errors of $\gtrsim 30\%$ if the same misguided assumption of the continuum slope were made. Errors in line-center continuum estimation of this magnitude could translate into severe errors in continuum subtraction of $\text{Ly}\alpha$ since the on-line bandpass is so broad: if the line does not dominate, then the continuum subtracted pixel could quite feasibly get the wrong sign (emission could be seen as absorption and vice versa). For a dust-free starburst the slope of the FUV continuum is largely constant $\beta \sim -2.6$ over the first few 10s Myr, but flattens quite rapidly (β increases) thereafter, particularly at higher metallicities (Leitherer et al. 1999). Since the UV slope is also a strong function of the dust reddening (E_{B-V}), it is not possible to reliably predict β globally, let alone how it varies on ~ 10 pc scales (i.e. pixel-to-pixel, at SBC sam-

¹Continuum is assumed to take the form of a power-law in λ of the form $f_\lambda \propto \lambda^\beta$

pling). One possible alternative would be to sample the blue and red sides of the on-line filter but there are no filters available for such an observation and spectroscopic observations with the *STIS* have shown that the continuum on the blue side of Ly α is frequently unpredictable, contaminated by internal or Galactic absorption features. Flux at Ly α due to continuum processes must be estimated from observations on the red-side of Ly α only.

The next step would be to take an additional off-line observation redwards of the off-line filter (e.g. *ACS/SBC/F150LP* or *F165LP*, *WFPC2/F218W* *ACS/HRC/F220W*, or *WFC3/UVIS/F225W*) and extrapolate a power-law continuum to the on-line filter. This way *CTN* would be computed for a given spectral slope by convolving the throughput profiles with the measured power-law, resulting in a different *CTN* in each pixel. However, this method was demonstrated to result in significant errors in the continuum flux estimation when relatively moderate amounts of dust are present (Hayes et al. 2005; Hayes & Östlin 2006) since typical dust reddening modifies the FUV continuum in such a way that it becomes inconsistent with the power-law approximation. Furthermore, such a method provides no estimate of stellar Ly α absorption which is significant in all but very hottest stars.

Naively, these points could be argued away: only the very youngest star-forming regions produce enough ionizing photons to generate significant Ly α (Charlot & Fall 1993) over which times β is essentially constant. High resolution imaging studies have however demonstrated that in the ISM of active starbursts, particularly surrounding massive young clusters, the nebular emission can be clearly displaced from the ionizing sources (e.g. Maíz-Apellániz et al. 2004). This is most likely due to stellar winds and supernova feedback clearing bubbles in the ISM and is clearly visible in some cases in our sample, well exemplified by ESO 338-IG04 (Östlin et al. 2009). The case is further complicated for Ly α by its resonant nature. As a result of multiple scatterings in H I , Ly α photons diffuse away from their production sites and are likely emitted from a site of last scattering that is not coincident with the nebulae where they were produced (Hayes et al. 2005, 2007; Östlin et al. 2009). ESO 338-IG04

(Hayes et al. 2005) shows a large diffuse emission component which dominates the total Ly α luminosity. High resolution imaging frequently reveals that starbursts are composed of numerous compact young knots and clusters that dominate the luminosity but do not account for a large fraction of the surface area (Meurer et al. 1995), particularly at UV wavelengths. It is therefore rather likely that the continuum that needs to be subtracted will not be representative of a region young enough to produce Ly α , which can emerge superimposed upon regions that appear too dusty for Ly α to be transmitted (Hayes et al. 2007).

Figure 2 demonstrates inadequacy of assuming a one-to-one relationship between *CTN* and β . Here the two quantities are computed for various ages and E_{B-V} by convolving *Starburst99* spectra (Leitherer et al. 1999; Vázquez & Leitherer 2005) with the filter throughput profiles. For this demonstration the Calzetti et al. (1994) attenuation law is adopted which is frequently used to represent dust extinction in starbursts and LBGs. The first example shows our own observing strategy using *SBC/F122M* for Ly α on-line, *SBC/F140LP* for off-line, measuring β between *F140LP* and *HRC/F220W*. The second example shows how, by adopting the *F125LP*, *F140LP* and *F150LP* configuration, the degeneracy in *CTN vs. β* is significantly reduced. However, with uncertainties still greater than 40% at certain β , it is still not sufficient for the broad on-line filter. In general the extinction laws of the Milky Way and Magellanic clouds are found to be steeper than the Calzetti et al. (1994) law at given E_{B-V} over the wavelength domain covered by our filters and the effect is found to be more severe.

2.2.2. Methods beyond pure observation

CTN is the only important quantity to know for the continuum subtraction but unfortunately, as demonstrated in Section 2.2.1, the quantity cannot easily be estimated without some knowledge of the continuum. A solution is compute *CTN* from spectral synthesis models using supplementary data to constrain the model. Thus one must have sufficient information at hand to build the right stellar population; stellar age and star-formation history, E_{B-V} , metallicity, and the initial mass function (IMF) may all have a significant effect.

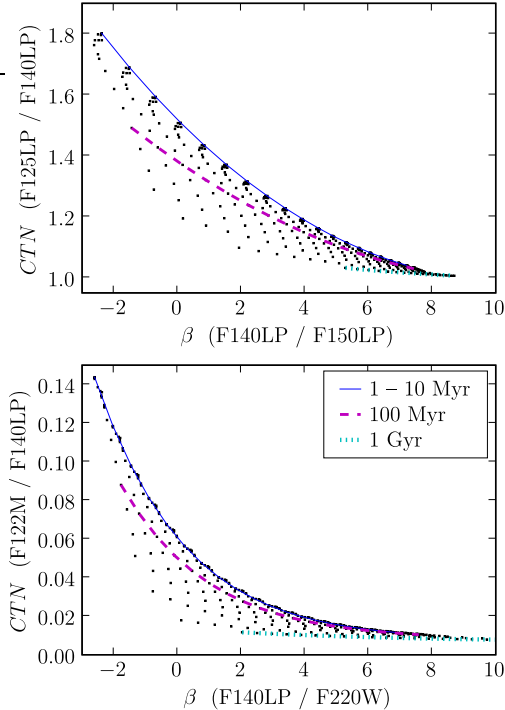


Fig. 2.— CTN vs. β for various ages (1 Myr to 1 Gyr) and E_{B-V} in the range 0 – 1 for the law of Calzetti et al. (1994). Lines link points of the same age (i.e. follow tracks of dust reddening). *Upper*: The configuration used for our current *HST* campaign. CTN is generated for $F122M/F140LP$ with β measured between $F140LP$ and $F220W$. CTN is clearly not a monotonic function of β and degenerate values of CTN can be derived for any measured β , especially for bluer colors (e.g. $\beta \sim -1$). *Lower*: Same as upper but for the configuration 2. CTN is generated for $F125LP/F140LP$ with β measured between $F140LP$ and $F150LP$. The degeneracy still exists although has been quite significantly improved.

In Hayes et al. (2005) we demonstrated that we could reliably continuum subtract $Ly\alpha$, pixel-by-pixel, in our *HST* observations (configuration 1) through multi-color spectral modeling using a number of additional broadband *HST* observations. In that study four line-free observations were used, together with the *Starburst99* spectral evolutionary models. In age- E_{B-V} space we showed that we could find non-degenerate solutions for CTN by sampling β (sensitive to both age and dust) and the Balmer/4000Å break (sensitive primarily to the age of the stellar population). Grids of multiple color indices and CTN were computed from the models for a range of age and E_{B-V} , enabling us to look up the most appropriate value of CTN in each pixel. We also demonstrated that several other parameters (metallicity, IMF, etc.) had only a small impact upon the reliability of the method. If χ^2 is defined as

$$\chi^2 = \sum_i [C \cdot m_i(t, E_{B-V}) - d_i]^2 \cdot W_i \quad (2)$$

where $m_i(t, E_{B-V})$ represents the i th model data point on the SED for given age (t) and E_{B-V} , C the model normalization factor, d_i flux measured in the i th filter, and W_i the weight for the corresponding filter, typically the inverse variance. The value of C that provides the best fit is determined from

$$C = \frac{\sum_i m_i d_i W_i}{\sum_i m_i^2 W_i} \quad (3)$$

where C and χ^2 are computed for each possible model spectrum, selecting the best models from the minimum value of χ^2 . Figure 3 shows an example χ^2 map in t - E_{B-V} space.

Naturally, if CTN is sensitive to the Balmer/4000Å break, then a number of contaminants may affect the CTN determination, depending upon how well the stellar and nebular emission regions are resolved. At the earliest times when the nebular emission is strong, the Balmer edge may contribute by bluening the restframe $U - B$ color. On the other hand, at later times the 4000Å break arises from metal line blanketing in late type stars, reddening $U - B$. Thus resolved nebular gas and old stellar populations may both affect the SED in the optical but not the FUV; not affecting CTN itself but its determination should optical SED

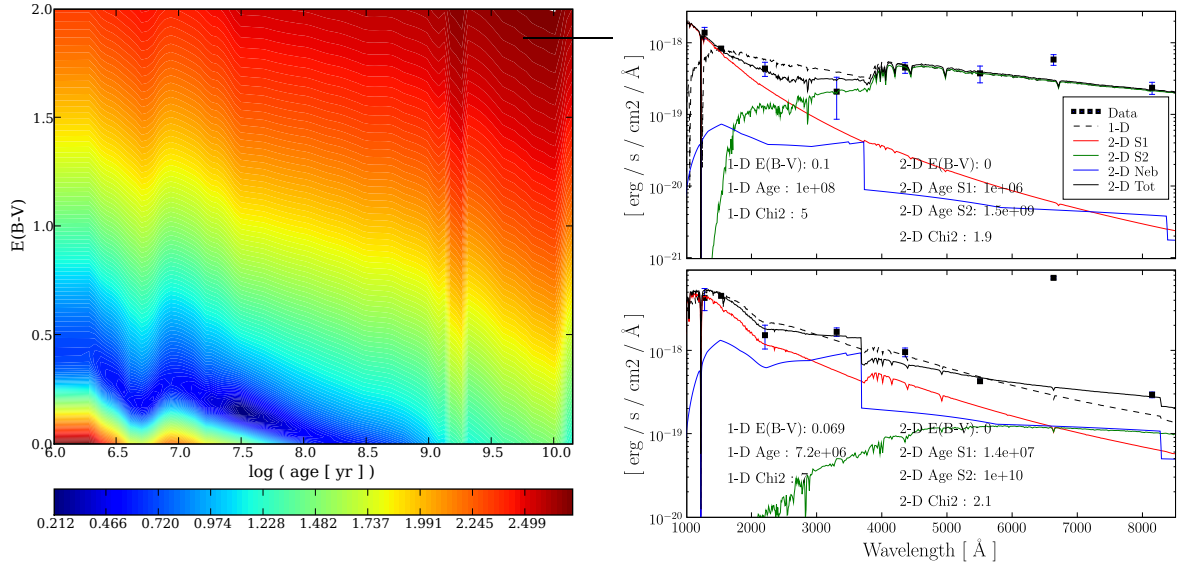


Fig. 3.— *Left*: $\log(\chi^2)$ map for a one component stellar fit of age and E_{B-V} . A degeneracy is clearly seen, running diagonally and negatively in age- E_{B-V} space although note the logarithmic scaling. Data for this plot is taken from a diffuse Ly α emission region in the vicinity of Knot B of Haro 11. *Upper right*: Example of a multi-component SED fitting to real data from Haro 11 (Hayes et al. 2007). Blue shows the nebular gas continuum spectrum, the level of which is determined from the H α observation (note the data point at H α is lies high above the fit, since this observation contains both line and continuum), green shows the underlying field-star population of age around 1 Gyr that dominates in the I -band, red shows the current starburst with an age of 1 Myr. Black shows the total combined spectrum. Dashed black line shows a single component spectral fit. *Lower right*: Same as *upper* but extracted from a well resolved H α shell in ESO 338-IG04 (Östlin et al. in prep.). The extremely high H α equivalent width is apparent since the stellar continuum is rather weak. The nebular continuum level is higher than that of the stars in the U and I bands. The data-points show the $U - B$ color is negative and the Balmer jump is significant in the total spectrum. The nebular component still does not contribute near Ly α but demonstrates why control over the nebular continuum spectrum is necessary.

data-points be relied upon. Since the relative contribution from stellar populations and nebular gas is unknown, and in high-resolution imaging the regions may be clearly resolved, it may become necessary to account for all these populations in our estimation of the true spectrum, and therefore *CTN*.

Control over the nebular gas contribution may be obtained through additional observations that directly trace the ionized gas. For given temperature in an optically thin nebula, the emission coefficients (α^{eff}) may be computed for any allowed recombination line, and continuous emission coefficient (γ_ν) computed for given wavelength. Thus an appropriately strong and well-behaved line (e.g. $H\alpha$) can be used to estimate the nebular continuum contribution in each filter, and subtract it from each data-point for a given E_{B-V} (again, the filters have been selected in order to avoid the strongest nebular emission lines). *CTN* may then be computed using the SED-fitting method to obtain the stellar-only SED (minimizing χ^2 using Equation 2) and reconstruction the composite spectrum.

The current starburst may be superimposed upon any underlying stellar population. Since this is likely to show a significant 4000Å break but little FUV contribution, it may affect the reliability of *CTN* determination that relies upon age fitting. Thus it may be necessary to treat more than one stellar population per pixel. Old stellar populations may dominate the integrated light at red wavelengths and such an observation may facilitate the decomposition of starburst and underlying stellar components. Equation 2 can be modified to include two populations, a and b , each with differing normalization as

$$\chi^2 = \sum_i [C_a \cdot m_{a,i} + C_b \cdot m_{b,i} - d_i]^2 \cdot W_i \quad (4)$$

where $m_{a,i}$ and $m_{b,i}$ represent the model SED data-points, with C_a and C_b the normalization factors for each population. For a given set of models m_a and m_b , an analytic solution exists for the values of C_a and C_b that provide the best-fit, as:

$$\begin{aligned} C_a &= \frac{S_5 S_2 - S_3 S_4}{S_2^2 - S_1 S_4} \\ C_b &= \frac{S_3 - C_a S_1}{S_2} \end{aligned} \quad (5)$$

where

$$\begin{aligned} S_1 &= \sum_i m_{a,i}^2 W_i \\ S_2 &= \sum_i m_{a,i} m_{b,i} W_i \\ S_3 &= \sum_i m_{a,i} d_i W_i \\ S_4 &= \sum_i m_{b,i}^2 W_i \\ S_5 &= \sum_i m_{b,i} d_i W_i \end{aligned} \quad (6)$$

With the contributions from the two stellar populations measured or fit, the total SED can be reconstructed by summing the SED in each component. Thus *CTN* is determined from the reconstructed model spectrum.

The fact that stellar ages may be estimated provides the first-order solution to another potential problem: that of the underlying stellar Ly α absorption feature. For O stars, and depending on the wind properties, Ly α can be expected in absorption, filled in P Cygni, or emission (net equivalent widths of a few Å are expected, Klein & Castor 1978). However, due to the deep Galactic HI column to even the nearest O stars, the intrinsic Ly α profile is completely absorbed and it is likely these predictions can never be empirically tested. Some B stars however are near enough to be observed at Ly α and NLTE atmosphere models appear to be able to match the observed profile (Ly α absorption equivalent widths of a few tens of Å). Since no observational tests are available, it is not deemed meaningful to pursue this issue further, although it is worth pointing out that the stellar feature is accounted for, within the limits of current understanding.

In the following Sections we assess the relative power of the various methods described above in recovering Ly α fluxes and equivalent widths.

3. Methodology and Tests

The aim of this study it to test how reliably we can recover Ly α observables from our imaging observations. Ideally we would like to test the various methods of continuum subtraction against real observational data for which the true Ly α fluxes and equivalent widths are known (i.e. spectra).

Unfortunately there are no real object spectra that span the wavelength range between Ly α and 9000Å with sufficient spectral resolution, taken in consistent apertures for us to test the various methods against real data, and we are forced to rely only upon synthetic input sources.

In this study we present a number of computational tests to assess the performance of various methods. To this end we generate a set of template spectra using various combinations of *Starburst99* models (Leitherer et al. 1999; Vázquez & Leitherer 2005), for various stellar populations (or combinations thereof), E_{B-V} , and modify them by adding Ly α lines of chosen equivalent width. We then convolve the template spectra with the *HST* bandpasses to generate synthetic SED data-points and feed these into our SED-fitting and continuum subtraction software. Thus we have full knowledge of the intrinsic spectrum, and we are able to compare our output results directly to the known input values (CTN , $F_{Ly\alpha}$, $W_{Ly\alpha}$), and test the ability of our fitting methods to recover ages and reddening in the stellar population(s).

We simulate noise by randomizing each SED point for a given error and, adopting a Monte-Carlo approach, we compute various statistics of the recovered distributions. For the real *HST* data we employ adaptive binning techniques to obtain a minimum threshold S/N , but the choice of this value requires testing. Therefore by performing these simulations we are able to test the results obtained against input S/N , and directly test the optimum threshold.

The method of generating the ‘real’ input spectra is outlined in Section 3.1. The various methods of subtracting the continuum are described in Section 3.2, and the actual quantitative tests are described in Section 3.3.

3.1. Input SED generation

We have previously discussed the fact that SED is likely to be the sum of the contributions from a current episode of star formation (starburst; **sb**), an underlying component of field stars (**fs**), and emission from nebular gas (**neb**). All template input spectra are generated from a combination of these three components, scaled to a given normalization relative to the starburst at 4500Å

($\sim B$ -band); these normalizations are assigned the n_{fs} and n_{neb} for the field stars and nebular components, respectively. The templates thereby consist of two stellar components of variable ages, and a single gas component, all contributing different fractions of the B -band luminosity. For simplicity, the two stellar components are generated from the same metallicity and initial mass function. The H α luminosity is computed from the nebular gas continuum flux density and applied to the gas spectrum before addition. To complete the restframe spectrum, it is reddened using a given extinction law and E_{B-V} . Finally the spectrum is redshifted. Further information on the generation of input spectra can be found in Section 3.3 and Table 1.

For each template spectrum, we generate a set of ‘observed’ SED data-points by convolving the spectra with the *HST* filter profiles. For configuration 1 (our current imaging campaign) the complete filter list is: *SBC/F122M* (Ly α on-line), *SBC/F140LP* ($\sim 1500\text{Å}$ continuum), *HRC/F220W* ($\sim 2200\text{Å}$ continuum), *HRC/F330W* ($\sim U$ -band), *WFC/F435W* ($\sim B$ -band), *WFC/F550M* (medium V -band, serving as line-free continuum filter near H α), *WFC/FR656N* (linear ramp narrow-band filter centered upon restframe H α), and *HRC/F814W* ($\sim I$ -band). For configuration 2 the filter set replaces *F122M* with *F125LP* while *F140LP* remains the FUV continuum filter as shown in Figure 1. For the optical component of this configuration we sample the UV/optical continuum using *WFPC2/F336W*, *F439W*, and *F814W*, using the fixed narrow-band filter *F673N* to observe redshifted H α .

3.2. Continuum subtraction methods

For each SED we apply various methods of estimating and subtracting the continuum and examine how well they return the known restframe quantities that were input. We identify five possible methods of estimating CTN and subtracting the continuum at Ly α :

- I Assuming the slope of the continuum between the off-line and on-line filters to be flat in f_λ . I.e. CTN is the ratio of the *HST* PHOT-FLAM values for each filter.
- II Assuming the continuum takes the form of a power-law in f_λ ($\propto \lambda^\beta$) and extrapolating

the slope as measured between the NUV filter at $\sim 2200 \text{ \AA}$ and the off-line FUV filter (*F140LP*).

- III Fitting a single *Starburst99* spectrum (combined stellar+nebular components) to the continuum SED points (i.e. excluding the $\text{H}\alpha$ observation) using Equations 2 and 3. Then computing *CTN* from the best-fitting (age and E_{B-V}) spectrum.
- IV Continuum-subtracting $\text{H}\alpha$ and using the $\text{H}\alpha$ flux to reconstruct the SED due to nebular continuum processes. Then fitting a single stellar-only *Starburst99* spectrum (again fitting age and E_{B-V}) to the real SED data-points with the nebular contribution subtracted (i.e. real data-points – nebular data-points) using the same method as method III.
- V Same as method IV but fitting 2 stellar components to the nebular-subtracted SED using Equations 4,5, and 6. In this case, the fitting is performed over all ages with age allowed to vary in *both* stellar populations.

3.3. The tests

The most important returned values are, of course, $F_{\text{Ly}\alpha}$ and $W_{\text{Ly}\alpha}$, although from methods where SED fitting is employed, age(s), normalization factor(s), and E_{B-V} are also returned. Monitoring these returned values in addition to those relating to $\text{Ly}\alpha$ permits a deeper examination of the performance of the SED fitting.

We begin by defining a fiducial template spectrum, denoted *fid*. This is generated from what is thought to be a typical starburst, capable of producing $\text{Ly}\alpha$ with moderate extinction and metallicity and a Salpeter IMF. For the starburst, a single stellar population of age of 5 Myr is selected since ionizing photons are a requirement for the production of $\text{Ly}\alpha$. According to the *Starburst99* template spectra, the nebular gas contribution at 4500\AA (n_{neb} , defined relative to the stellar spectrum of an unresolved point-source) is ~ 0.05 at this age, and this value provides the fiducial n_{neb} . For the fiducial model we add a moderate field-star population with age (arbitrarily selected) 5 Gyr, scaled to give a contribution of 50% the starburst luminosity at 4500\AA ($n_{\text{fs}}=0.5$).

The fiducial reddening for the composite spectrum was selected to be $E_{B-V}=0.2$ using the SMC law. The value of E_{B-V} is an approximate midpoint in the measured extinction for most of our galaxies (see Atek et al. 2008). The choice of law is motivated by the fact that the SMC law appears to provide the best fits to the resolved spectra of blue compact and irregular galaxies (e.g. Mas-Hesse & Kunth 1999). Since $W_{\text{Ly}\alpha}$ can essentially take any value between damped absorption and super-recombination values, we add $\text{Ly}\alpha$ lines with a range of equivalent widths: -50\AA to represent the deep absorption seen in some local objects (e.g. *1Zw18*); 0\AA , corresponding to no $\text{Ly}\alpha$ feature; 10\AA to approximate the global values measured in some of low- z objects (e.g. Giavalisco et al. 1996); and 100\AA corresponding to high- z $\text{Ly}\alpha$ -bright galaxies or diffuse emission regions in resolved objects at $z \approx 0$. We define a number of modifications to all of the ingredient parameters in the input spectrum which are listed in Table 1.

Firstly, all tests are performed at infinite S/N to test the reliability of the code by insuring all the input parameters are returned.

Observational S/N per resolution element varies significantly with position as a result of natural morphological variation in surface brightness, and band-to-band as morphology differs with wavelength. In our *ACS* data-set we make use of adaptive binning to bin together pixels until a threshold S/N has been met, conserving surface brightness in each conglomerate bin (“spaxel”). Without investigation it is not possible to know what S/N is required in order for the various techniques to become optimal; either converging on the input values or to some systematically offset values. By varying S/N in our simulations, we are able to test this directly. To each data-point in the input SED (see Section 3.1), we assign an error, based upon the S/N we want to test. Using this error we then regenerate 1000 SEDs using Gaussian-variates and apply all our continuum subtraction methodologies to each one. Performing such Monte-Carlo simulations with increasing S/N allows us to investigate the optimum S/N required to return mean values consistent with the those input, or find convergence of the mean to systematically offset observables. For each of the model galaxy SEDs defined in Table 1, we run

TABLE 1
PARAMETERS FOR SED GENERATION

Parameter	Unit	Fiducial value	Non-fiducial / Range	Code
$W_{Ly\alpha}$	Å	10	-50, 0, and 100	[fid_w10; fid_w-50; fid_w0; fid_w100]
E_{B-V}	mag	0.2	0.0 and 0.5	[ebv0_w...; ebv05_w...]
Reddening law	—	SMC	Calzetti et al. (1994)	[cal_w...]
Starburst age	Myr	5	20 and 100	[agesb20_w...; agesb100_w...]
Field star age	Myr	5000	200	[agefs200_w...]
n_{fs} ¹	—	0.5	0 and 5	[nfs0_w...; nfs5_w...]
n_{neb} ²	—	0.05	0 and 1	[nneb0_w...; nneb1_w...]
IMF α	—	-2.35	-1.85 and -2.85	[imf185_w...; imf285_w...]
Metallicity	Z	0.08	0.001 and 0.040	[metsub_w...; metsuper_w...]
Stellar atmosphere ³	—	Atm5	Atm3 and Atm4	[atm3_w...; atm4_w...]
Redshift	—	0.01	—	—

NOTE.—Model parameters in the third column constitute the fid_w10 fiducial template spectrum case, with the non-fiducial values for $W_{Ly\alpha}$ constituting standard cases of fid_w-50, fid_w0, and fid_w100.

¹ defined relative to Starburst population at 4500Å (i.e. \sim relative B -band luminosity).

² defined relative to Starburst population at 4500Å. 0.05 corresponds to typical default unresolved nebular fraction at 5Myr from *Starburst99*. 0 and 1 correspond therefore to zero nebular contribution and a ‘boost’ by a factor of ~ 20 .

³ Designated *Starburst99* codes. Atm3 is Lejeune atmospheres for stars with plane-parallel atmospheres and Schmutz atmospheres for stars with strong winds. Atm4 is like Atm3 but with Hillier atmospheres for stars with strong winds. Atm5 is like Atm4 with Pauldrach models for O stars.

1000 Monte-Carlo iterations at each S/N with S/N varying between 1 and 50. Important statistics of $F_{Ly\alpha}$ and $W_{Ly\alpha}$; the mean and median, standard deviation, and skewness of the derived distribution are retained.

Firstly we set S/N to be the same in all bandpasses; if the worst quality band is chosen to generate the binning pattern, S/N in the corresponding bins in other bands should have S/N exceeding the threshold. However, due to differing morphologies, this is unlikely to be the case in general, and some bins, in some images, may fall short of the desired S/N threshold. We assess the impact of this to the overall fitting by systematically dropping S/N to zero in individual bands for the fiducial SED. This allows us to examine the robustness of returned Ly α -related quantities in the case where lower-quality data have been obtained in certain bandpasses. Similar tests are then performed dropping S/N to zero in adjacent pairs of filters simultaneously.

To test the reliability of the methods for a wide array of model galaxies we augment the fiducial SED, one parameter at a time, always running the SED-fitting and continuum subtraction code using the standard *Starburst99* parameters and SMC reddening law. Age and reddening, of course, are always the free parameters in the fitting (both age

components are fit for method v). This way we can assess the reliability of our results at different stellar ages, E_{B-V} , and with different contributions from the underlying stellar population and nebular gas. The same is also true when we test metallicity, IMF, reddening law, enabling us to test the impact of failing to select the correct values for the fitting. The effect of metallicity is found to be have sufficient impact that additional tests are performed, see Section 4.2.3. The parameter space covered is listed in Table 1. Parameter dependency tests are performed for both observational configurations with a detailed discussion of the results for configuration 1, including the effects of poor S/N in certain filters, presented in Sect 4. A summary of the results for configuration 2 is presented in Sect 5.

4. Results and discussion

4.1. The fiducial model

In this subsection we first present and discuss the results obtained for the fiducial SED with the same S/N in all bandpasses in Sect 4.1.1, followed by results where single and adjacent pairs of filters have $S/N = 0$ in Sect 4.1.2.

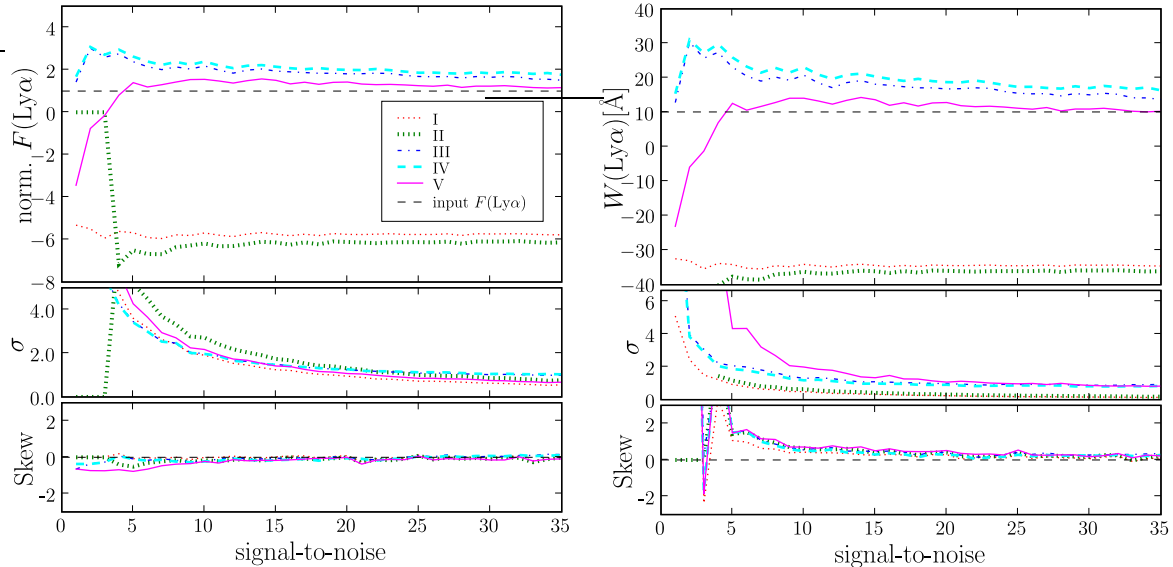


Fig. 4.— Statistics of the returned distribution from 1000 Monte-Carlo iterations on the fiducial setup with $W_{\text{Ly}\alpha}$ of 10\AA . *Top* panels show the mean, *center* the 1σ standard deviation, and *lower* the skewness. *Left*: Continuum subtracted Ly α flux in normalized units (i.e. returned mean divided by input flux). Standard deviation is also given in normalized units. *Right*: Ly α equivalent width. Colors, line styles, and weights show the various methods of estimating the continuum and are labeled in the legend.

4.1.1. Equal S/N in all bands

Figure 4 shows the returned statistics for the fiducial model as a function of S/N . Statistics shown include the mean (*upper*), standard deviation (*center*), and skewness (*lower*). Firstly, these plots demonstrate that simple assumptions about the continuum slope (either $\beta = 0$ (method I) or β extrapolation (method II)) both result in an overestimate of CTN . Therefore the continuum is over-subtracted and a 10\AA emission line is seen as an absorption feature with $W_{\text{Ly}\alpha} \sim -40\text{\AA}$. This is the result of: (a) the large offset in λ between the off- and on-line filters; (b) the fact that the $\sim 100\text{\AA}$ wide on-line bandpass is far from line-dominated; and (c) the modest value of $E_{B-V} = 0.2$ is sufficient to reduce the total flux in $F122M$ below that of $F140LP$. It is clear that a good understanding of the continuum is essential, not only between the filters but across the on-line bandpass itself, and that spectral modeling of some level of sophistication is a requirement. It should be noted that at $S/N = 10$ in the individual bandpasses, S/N in the continuum subtracted Ly α distribution is only around 0.5, although obviously this

improves with increasing $W_{\text{Ly}\alpha}$ as the line starts to dominate. For the `fid_w100` case, $S/N = 4$ is seen in the returned Ly α flux distribution for $S/N = 10$ in all filters. Of the three SED-fitting methods, technique v slightly out-performs III and IV, thanks to its inclusion of treatment of the underlying stellar population and nebular gas, even though they are only minor contributors to the FUV flux for the `fid` SED. It should also be noted that all the continuum subtraction methods show a positive skew in the $W_{\text{Ly}\alpha}$ distribution, even at $S/N > 30$. This is due to fact that W is a ratio, and that the inverse of a Gaussian distribution always shows positive skewness – this should be present in all equivalent width estimates, irrespective of data-set or observational methodology (for a discussion see Dawson et al. 2004; Hu et al. 2004; Hayes & Östlin 2006).

An estimate of the age of the stellar population also provides, in part, the solution to another potential problem, that of the unknown underlying stellar absorption at Ly α . While still poorly tested, Ly α features in the models still provide the best estimate of the underlying absorption avail-

able and are included in computed values of CTN and therefore the estimate of the continuum flux.

4.1.2. Reduced filter sets or poor S/N

The upper panel of Figure 5 shows the effect of removing a single filter from the fitting routine for the `fid_w10` SED. Naturally, only the three continuum subtraction methods that employ SED fitting are shown. We now show the mean $W_{Ly\alpha}$ obtained with the filter removed, normalized by that obtained with all filters included, with the same S/N in all included bandpasses. This normalized distribution has clearly been shown to converge in flux at $S/N \approx 5$ (Figure 4). The results are noisier than those shown previously for two reasons: firstly because the fits are intrinsically noisier due to one fewer data-point being present, and secondly because of added noise from the normalization. The example shown illustrates the removal of the $F220W$ filter, although results are largely indistinguishable when other single filters are removed. This is because we have a maximum of 5 model parameters to fit and in the case where a single filter is removed, we still have sufficient data-points remaining to avoid a degeneracy. Provided we obtain the minimum S/N threshold of 10 as shown in Section 4.1.1 in 5 of our 6 continuum bandpasses, we can feel safe about the recovery of $Ly\alpha$ fluxes.

The situation changes, however, when two filters are removed from the fit as can be seen in the lower panel of Figure 5. This plot shows the same as the upper panel when the two UV filters ($F220W$ and $F330W$) are assigned $S/N = 0$. The two single stellar component fitting methods (III and IV) now consistently overestimate $W_{Ly\alpha}$ by around 20% at $S/N \sim 10$ which actually becomes worse as S/N increases in the other filters. This is due to more consistent selection of the wrong stellar parameters by the code and the example has been selected to show poorly recovered observables; the loss of both UV filters is the most detrimental. Without either $F220W$ or $F330W$, we have no sampling of the FUV continuum slope or the Balmer/4000Å break, essentially resulting in the recovery of any ages and E_{B-V} . Clearly maintaining $S/N \sim 5$ sampling of the Balmer break is preferable to obtaining extremely high S/N observations in other bandpasses; as discussed in Wiklind et al. (2008) the Balmer break is instru-

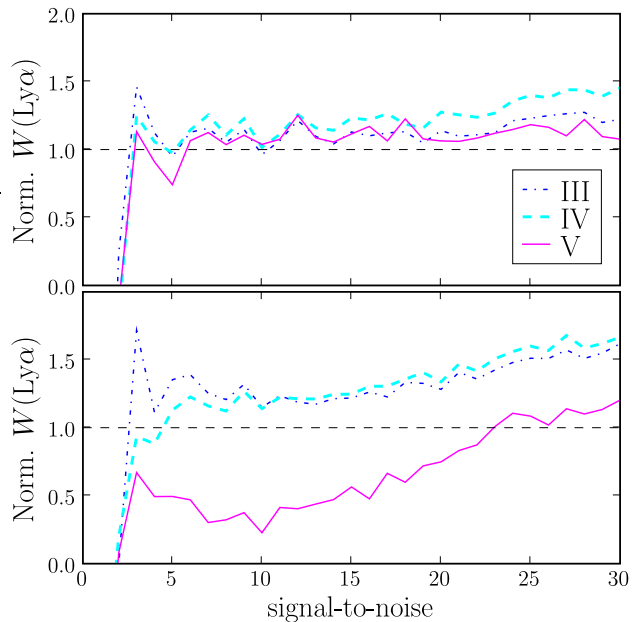


Fig. 5.— Average values of $W_{Ly\alpha}$ returned by the SED fitting software for the fiducial model galaxy with $W_{Ly\alpha}=10\text{\AA}$ when datapoints are removed from the fitting procedure. S/N is the same in all the remaining bandpasses. $W_{Ly\alpha}$ is now normalized by its value when all filters are included, where convergence was previously found after $S/N \sim 5$ (see Figure 4). The *upper* panel shows the removal of the $F220W$ filter. The removal of both $F220W$ and $F330W$ is shown below.

mental in resolving the degeneracy between age and reddening. We cannot conclude that methods III and IV out-perform V in this case but we can be quite certain that we need to reach the threshold S/N in 5 of our 6 continuum bandpasses in order for any of the SED-fitting methods to yield robust results. Four filters is not deemed to be sufficient for method V.

4.2. Parameter dependencies

We now assess the impact of modifying the various parameters that go into the construction of a the composite galaxy spectra. The fiducial parameters are always used internally for the fitting (third column in Table 1), fitting only ages and E_{B-V} .

4.2.1. Stellar ages and dust reddening

Table 1 shows the various parameter modifications made to the `fid` galaxy template for starburst age, field star age, and E_{B-V} . For the SED-fitting methods (III, IV, and V) results are found not to be significantly discrepant from those presented for the fiducial case. In fact, aside from details in the noise, the flux and equivalent width plots are indistinguishable from those in Figure 4. This is not the case for methods I and II which vary wildly with starburst age and E_{B-V} . Naturally the behavior of the modeling methods is to be expected since age and E_{B-V} are our primary fitting parameters and the effect of dust can be well controlled in the event that the chosen extinction law well describes the intrinsic deviation from the dust-free starburst.

Exchanging the SMC extinction law for the attenuation law of Calzetti et al. (1994) is more detrimental: these two curves are not near equivalent over the wavelength domain we are sampling. For the `cal_w10` case, techniques III and IV result in convergent $W_{Ly\alpha}$ estimates of 75 and 112Å respectively while method V converges at $W_{Ly\alpha}=20\text{\AA}$ by $S/N = 10$ (still an overestimate by a factor of 2). For strong emission (`cal_w100`), method V overestimates $W_{Ly\alpha}$ by just 10% at $S/N = 10$ while III and IV still consistently fail by a factor of 2. However, clearly an accurate model of the internal extinction law in the target galaxy is a key parameter in the method.

Several solutions to this exist. Firstly, the red-

dening law itself could be incorporated as a free parameter, only increasing computation time by a factor of a few. Including individual extinction laws (e.g. SMC, LMC, or Galactic curves) in the SED fitting is physically rather poorly motivated and a better alternative may be to base the choice of law on observation. For example FUV spectroscopy of the objects could indicate the presence or absence of a 2175Å graphite feature to motivate the choice of curves (see Puget & Leger 1989 and the discussion in Mas-Hesse & Kunth 1999).

4.2.2. Nebular gas and underlying stellar population

Figure 6 shows the average returned $W_{Ly\alpha}$ as a function of S/N when the nebular gas component contributes equally with the starburst at 4500Å (`nneb1_w10`; *left*), and when the underlying population contributes 5 times that of the starburst (`nfs5_w10`; *right*). The left plot demonstrates how a single component fit (III) breaks down in the `nneb1_w10` model when the nebular gas component is dominating the SED (i.e. regions where wind-blown HII shells or filamentary structure are resolved). Method III converges with a returned $W_{Ly\alpha}$ of around 40Å in this case, and a similar arithmetic (+30Å) overestimate for all the input equivalent widths. This demonstrates the need for an independent measure of the nebular gas spectrum as methods IV and V well recover $W_{Ly\alpha}$.

The right plot shows the necessity to also control the underlying stellar population when fitting stellar ages. The ordinate axis does not show methods III or IV which both converge at $W_{Ly\alpha} \sim 200\text{\AA}$. This corresponds to an overestimate of an order of magnitude, with overestimates seen for all input $W_{Ly\alpha}$. Notably, $W_{Ly\alpha}$ converges at around 400Å in the `nfs5_w100` case and almost +100Å in the `nfs5_w-50` case using methods III and IV.

4.2.3. Metallicity

Two additional metallicities were initially tested: the minimum sub-solar value ($Z = 0.001$; `metsub`) and maximum super-solar value ($Z = 0.040$; `metsuper`). The *upper* panel of Figure 7 shows the returned values of $W_{Ly\alpha}$ for the models with modified metallicities `metsub_w10` and `metsuper_w10`, again normalized by the returned

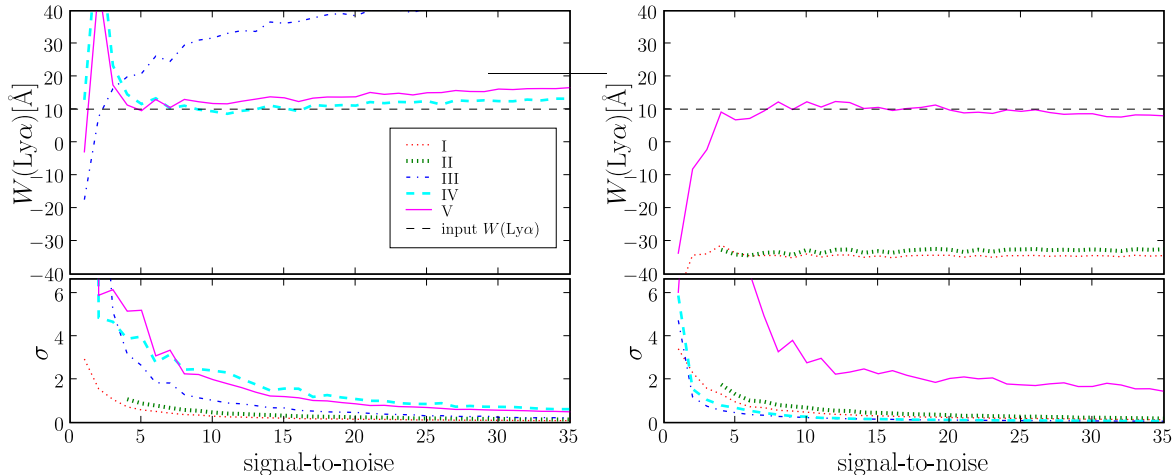


Fig. 6.— As in the right panel of Figure 4 but with different input parameters. *Left*: `nneb1_w10` in which the starburst and nebular gas component contribute equally at 4500\AA . Methods I and II both converge significantly off the lower end of the ordinate axis. *Right*: `nfs5_w10` in which the field star population outshines the starburst at 4500\AA by a factor of 5. Methods III and IV both converge significantly off the ordinate axis at equivalent widths of almost 200\AA .

values for the `fid_w10` model as described for Figure 5. Interestingly, while one represents a decrease in metallicity and one an increase, both modifications have a similar impact on the resulting observables: the continuum flux in the on-line filter is consistently underestimated. The underestimate is around 5% in the both cases but, for the weak emission cases this is enough to cause overestimates in $W_{\text{Ly}\alpha}$ of 10\AA (a factor of 2) using method V and worse for III and IV. The effect is less noticeable in the cases of stronger $\text{Ly}\alpha$ emission where the underestimate of the on-line continuum flux linearizes and converges to overestimates proportional to the error on the continuum. In a similar manner to when filters were removed from the fit (Sect. 4.1.2), increasing S/N means that unrepresentative fits are found more consistently, resulting in less spread in the output values than at low S/N where the spread is the result of noisy fits. In the case of metallicity, poor recovery of stellar age is found to be the culprit behind deviant $\text{Ly}\alpha$ observables due to the impact of metallicity on the 4000\AA break.

The apparent strong effect of unconstrained metallicity appears to be a concern and has prompted further tests. In the second round of testing, all available metallicities were exam-

ined; $Z = [0.001, 0.004, 0.008, 0.020 \text{ and } 0.040]$. A set of template spectra was generated for each one, and each model galaxy was run through the continuum-subtraction software five times, once for each metallicity. As demonstrated, quite significantly inaccurate results can be returned if the contrast between real and assumed metallicity is large (factors greater than around 2). However, using method V and for all cases with weak $\text{Ly}\alpha$ emission ($W_{\text{Ly}\alpha}=10\text{\AA}$), the discrepancy in $\text{Ly}\alpha$ fluxes is reduced to less than the returned statistical error-bar provided that (a) metallicities are not discrepant by more than one adjacent step in the grid, and (b) $S/N = 5$ or greater has been obtained in all bands. Fortunately, very strong metallicity gradients are not often found across starburst regions and a single long-slit spectrum is likely to provide sufficient information.

4.2.4. The initial mass function

The lower panel of Figure 7 shows the normalized returned values of $W_{\text{Ly}\alpha}$ for the models with modified IMFs: the flatter `imf185_w10` and the steeper `imf285_w10`. IMFs are modified in both the starburst and underlying stellar components for the generation of the template spectra. Methods III and IV here appear to perform in a simi-

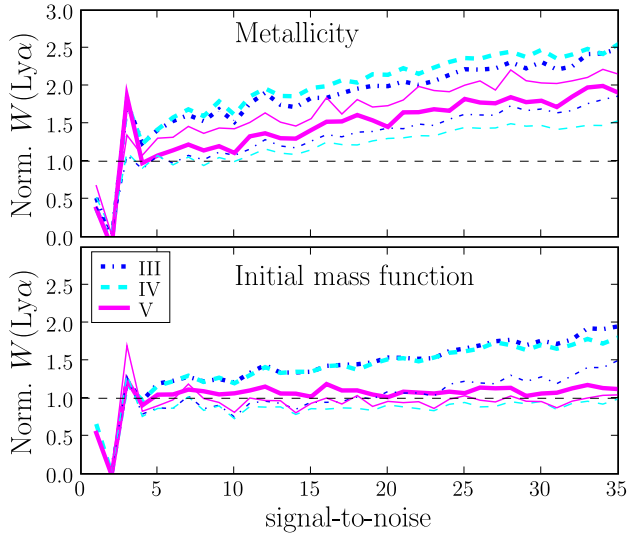


Fig. 7.— As in Figure 5 for different metallicities (*upper*) and initial mass functions (*lower*). Input $W_{\text{Ly}\alpha}$ is 10\AA . SED-fitting methods only are shown and methods are labeled. $W_{\text{Ly}\alpha}$ is normalized by the resulting values obtained from the fiducial model, output values of which have previously been shown to converge at around $S/N \sim 5$. For metallicity, the thick lines represent sub-solar and the thin lines super-solar metallicity. Regarding the IMF, the thick lines show the flatter `imf185_w10` model while the thin lines show the steeper `imf285_w10` model.

lar manner to when metallicity is modified: normalized $W_{\text{Ly}\alpha}$ deviates further from unity with increasing S/N as poor fits are consistently found. However, the two-component stellar fit method always recovers a mean $W_{\text{Ly}\alpha}$ that scatters around the 1-line. This results from the fact that IMF and star-formation history both alter the current stellar mass distribution: fitting two components appears to mimic the effect of a singly modified IMF.

4.2.5. Stellar atmosphere

Changing the UV stellar atmosphere model makes no appreciable difference to any of the methodologies. All SED-fitting methods appear to return $W_{\text{Ly}\alpha}$ consistently around the desired value and results are indistinguishable from those presented in Figure 4. While testing one stellar atmosphere model against another in this manner may not be greatly meaningful, it is at least reassuring that the choice of atmosphere does not impact upon the recovered values. The stellar atmosphere models differ quite significantly in their ionizing output and in the detail of line features. However the ionizing output only affects the nebular fluxes which are treated independently, and the discrete line features have only a minor impact upon integrated colors, even in the FUV.

5. Future studies and possible further improvements

So far we have only discussed simulations relating to the data-sets we have already obtained, targeting the lowest redshifts possible. However, this redshift severely limits the number of potential target galaxies, and any future Ly α imaging studies will require larger volumes, especially in order to target the more luminous analogues of high- z star-forming galaxies. Beyond $z \approx 0.03$ the optimal choice of filters changes, and can be performed using *ACS/SBC* and adjacent pairs of long-pass filters. Here we present some simulations for such a study. We also discuss some methodological alternatives using augmented datasets.

5.1. A potential local Ly α imaging study with HST

As discussed in Sect. 2.1 and illustrated in Fig. 1, we adopt the combination of *F125LP/F140LP*,

restricting us to the broad redshift range of $0.028 - 0.09$, although any adjacent pair of long-pass filters can be used. With the current inactive status of *ACS* CCD channels and uncertain future of *WFC3*, we opt for bandpasses available on *WFPC2* to cover the optical domain, although this setup could easily be ported to configurations on both these cameras. Filters chosen for the continuum and $H\alpha$ observations are listed in Section 3.1. It is also worth noting that with this configuration, we have no medium-band line-free filter near $H\alpha$ and the continuum subtraction of $H\alpha$ must rely on interpolation between *F439W* and *F814W*. Simulations presented here adopt the redshift $z = 0.029$ so as to shift $Ly\alpha$ into the on-line bandpass without shifting $H\alpha$ out of *F673N*.

Figure 8 shows some example results from simulations using configuration 2. They are the same results as shown for configuration 1 in Figure 6. These Figures show the recovered $Ly\alpha$ equivalent width from the nebular gas dominated and field-star dominated templates, and are highly reminiscent of those presented for configuration 1. Configuration 2 has the slight advantage over 1 of using two filters with near-identical red wings, which isolates a well-defined on-line bandpass shifted slightly nearer to the pivotal wavelength of the continuum measurement. However, configuration 2 does still suffer from the same drawback of a wide on-line bandpass and, for $S/N = 10$ in all bands, S/N in the continuum subtraction is still around 0.5 for the `fid_w10` model, the same as configuration 1 (Section 4.1.1).

Configuration 2 does include two fewer continuum filters than 1, which was previously shown (Section 4.1.2 and Figure 5) to be inadequate: the lower panel shows how $W_{Ly\alpha}$ is very poorly recovered when the NUV and U -band filters are removed. This was designed to exemplify the poor recovery of $Ly\alpha$ observables and this case was especially bad due to the loss of both UV filters, and no sampling of the FUV slope or Balmer/4000Å break. The inclusion of both *F220W* and *F330W* for configuration 1 is likely to include some level of redundancy. The continuum filters of configuration 2 are ideally placed and the most important spectral features remain well sampled: *F140LP+F336W* samples β , *F336W+F439W* samples the Balmer/4000Å

break, and *F439W+F814W* simultaneously allows for the continuum subtraction of $H\alpha$ and the constraint of the field star population. In light of these results and those presented in Section 4.1.2, we determine this to be the absolute minimum requirement in SED coverage.

5.2. Stellar and nebular extinction

One area in the methodology that could be identified as a weakness is the treatment of reddening: we treat stellar ($E_{B-V,\star}$) and interstellar extinction ($E_{B-V,IS}$) in the same, possibly sub-optimal, way: by locking them together. $E_{B-V,\star}$ and $E_{B-V,IS}$ are known to differ quite substantially in some cases, with derived values of $E_{B-V,\star}$ lower than $E_{B-V,IS}$ (Fanelli et al. 1988; Calzetti et al. 1994). This seems to be a geometric effect due to winds from massive stars expelling the ionized ISM and dust, reducing the extinction derived from the stellar UV slope and concentrating the dust in the HII shells and filamentary structures (Maiz-Apellaniz et al. 1998). Mas-Hesse & Kunth (1999) found that the discrepancy grew with increasing age over timescales consistent with stellar evolution and supernova enrichment. It is frequently the case that we can resolve nebular structure down to the resolution limit, although we will never know the geometry along the line-of-sight. How the dust in front of stars and in ionized regions combine depends upon the unresolved ISM geometry and it may, in such cases, be preferable to treat nebular and stellar reddenings independently in the method.

Decoupling could be achieved simply in the fitting procedure, by introducing $E_{B-V,IS}$ as an extra fitting dimension that applies only to the nebular SED, allowing both values of E_{B-V} to vary independently. However, the number of SED data-points is not sufficient for the inclusion of an extra degree of freedom, and currently we deem this too computationally expensive to include in the fitting algorithm when we have $\gtrsim 10^6$ pixels per image. While an empirical relationship has been presented between the two quantities by Calzetti et al. (2000): $E_{B-V,\star} = (0.44 \pm 0.033) E_{B-V,IS}$, it was derived for a sample of galaxies observed with much poorer resolution and, in individual *HST* pixels, the spread between the quantities is likely to be so large that the two quantities are completely decoupled. Alterna-

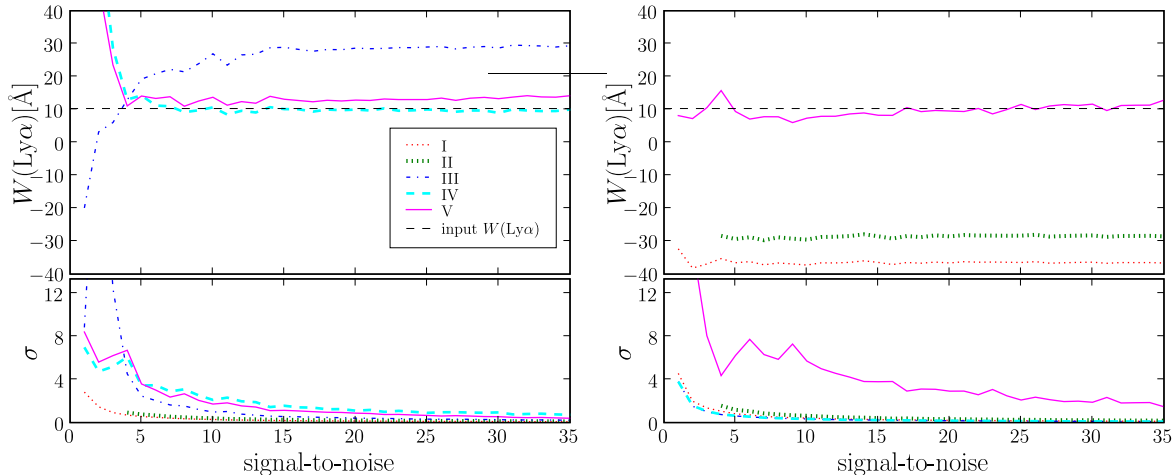


Fig. 8.— Example results using observing configuration 2. Input $W_{\text{Ly}\alpha}$ is 10\AA . *Left*: nebular emission-dominated region (`nneb1_w10`). Again, methods I and II converge well below the lower limit of the ordinate. *Right*: region dominated by and old stellar population (`nfs5_w10`). Methods III and IV converge above the upper limit of the ordinate. All continuum subtraction methods are shown and color-coded as in Figure 6.

tively, $E_{B-V, \text{IS}}$ may be measured directly by using an emission line decrement. Typically the Balmer decrement $\text{H}\alpha/\text{H}\beta$ would be used where $\text{H}\beta$ could also be obtained from *HST* using linear ramp or selected narrowband filters. A further possibility would be to use a NIR emission line (e.g. $\text{Pa}\alpha$ or $\text{Br}\gamma$) observed from the ground using a large adaptive optics imager. Indeed, an independent evaluation of the nebular reddening is precisely what is required for an appropriate astrophysical comparison with $\text{Ly}\alpha$. A direct measurement of the interstellar reddening would permit us to lock $E_{B-V, \text{IS}}$ on the nebular gas component and fit $E_{B-V, \star}$ to the stellar continuum. To this end we are in the process of observing a subset of our current sample in the $\text{Br}\gamma$ line. Such methods will be tested in a forthcoming study.

Ultimately, however, the continuum we need to estimate and subtract is predominantly stellar, and it may simply be that treatment of reddening on the stellar continuum is all that is required. Further dedicated tests will be presented when the data have been acquired and processed.

6. Conclusions and Summary

Using synthetic spectra of starburst galaxies we have examined various methods of producing continuum subtracted line-only $\text{Ly}\alpha$ images using

currently available imaging modes on the *Hubble Space Telescope*. We have assessed and compared various methods of continuum subtraction that vary in their complexity and attention paid to possible behavior of the continuum. We have presented examples covering a wide array of starburst parameters for two observational configurations: our *ACS/SBC* imaging campaign of local starbursts (online/offline = *F122M* / *F140LP*), and for studies using adjacent pairs of long-pass filters (*F125LP* / *F140LP*), targeting slightly higher- z . Our main conclusions are:

- Making simple assumptions about the shape of the far ultraviolet continuum slope (β ; e.g. assuming its slope or extrapolating the slope from observations on the red side only) leads to estimates of the $\text{Ly}\alpha$ flux and equivalent width that are seriously discrepant with the true values. Some spectral fitting is shown to be essential, even for the most basic cases.
- In our methodology we fit only the age of the stellar population and the dust reddening, requiring at least datapoints on the SED that sample the UV continuum slope and Balmer/4000 \AA discontinuity. All other parameters (extinction law, metallicity, IMF etc.) take assumed values; we then investigate the systematic effects incurred when

these quantities differ from their true values.

- We need to bin together pixels until signal-to-noise of between 5 and 10 has been obtained.
- Age determinations may be contaminated by boosted nebular gas emission and an underlying stellar population. These can be accounted for by constraining the nebular gas contribution using an estimate based upon the H α emission flux, and contribution from old stars by fitting multiple stellar components, respectively. This requires a data-point redwards of H α , both for the continuum subtraction of H α and an estimate of the contribution from field stars. We have determined the I -band to be functional.
- The initial mass function is shown not to be a necessary parameter to include in the fitting process and results are largely unchanged when non-standard IMFs are tested. Metallicity has a much more significant impact upon the recovery of the Ly α flux, since it changes the rate of stellar evolution and reddens stellar continua. This requires an independent determination of the metallicity. The choice of stellar atmosphere model has no discernible impact upon the recovered Ly α observables.
- If the metallicity and reddening law are known quantities and $S/N = 5$ has been obtained in all bandpasses, no significant systematic effects are seen in our continuum subtracted fluxes or equivalent widths. Increasing S/N to 10 is shown to significantly reduce the scatter. For input $W_{Ly\alpha}=10\text{\AA}$, we are able to recover Ly α fluxes accurate to within 30% of the true value for all tested parameter space. This improves to better than 10% for stronger Ly α emission with $W_{Ly\alpha}=100\text{\AA}$.
- We have also presented simulations for a very similar study that uses adjacent combinations of *SBC* long-pass filters to isolate Ly α . Due to the near-identical red wings, this could naively be thought to mitigate many of the issues surrounding continuum

subtraction. However, due to the broad nature of the bandpass, we still determine a similar level of care to be necessary in the method.

MH and GÖ gratefully acknowledge the support of the Swedish National Space Board (SNSB; Rymdstyrelsen) and Swedish Science Council (Vetenskapsrådet; VR). JMMH is supported by Spanish MEC grant AYA2004-08260-C03-03. We thank Hakim Atek for thoughtful comments on the manuscript, and Claus Leitherer and Artashes Petrosian for their invaluable contribution to the ongoing projects.

Facilities: HST (ACS).

REFERENCES

- Ahn, S.-H. 2004, ApJ, 601, L25
- Ajiki, M., et al. 2003, AJ, 126, 2091
- Atek, H., Kunth, D., Hayes, M., Ostlin, G., & Mas-Hesse, J. M., 2008, ArXiv e-prints, 805, arXiv:0805.3501
- Bergvall, N., & Östlin, G. 2002, A&A, 390, 891
- Calzetti, D., Kinney, A. L., & Storchi-Bergmann, T. 1994, ApJ, 429, 582
- Calzetti, D., Armus, L., Bohlin, R. C., Kinney, A. L., Koornneef, J., & Storchi-Bergmann, T. 2000, ApJ, 533, 682
- Cappellari, M., & Copin, Y. 2003, MNRAS, 342, 345
- Cardelli, J. A., Clayton, G. C., & Mathis, J. S. 1989, ApJ, 345, 245
- Charlot, S., & Fall, S. M. 1993, ApJ, 415, 580
- Charlot, S., & Fall, S. M. 2000, ApJ, 539, 718
- Dawson, S., et al. 2004, ApJ, 617, 707
- Dickey, J. M., & Lockman, F. J. 1990, ARA&A, 28, 215
- Diehl, S., & Statler, T. S. 2006, MNRAS, 368, 497
- Dijkstra, M., Wyithe, J. S. B., & Haiman, Z. 2007, MNRAS, 379, 253

- Fanelli, M. N., O'Connell, R. W., & Thuan, T. X. 1988, *ApJ*, 334, 665
- Giavalisco, M., Koratkar, A., & Calzetti, D. 1996, *ApJ*, 466, 831
- Hansen, M., & Oh, S. P. 2006, *MNRAS*, 367, 979
- Hayes, M., Östlin, G., Mas-Hesse, J. M., Kunth, D., Leitherer, C., & Petrosian, A. 2005, *A&A*, 438, 71
- Hayes, M., & Östlin, G. 2006, *A&A*, 460, 681
- Hayes, M., Östlin, G., Atek, H., Mas-Hesse, J. M., Jimenez, E. et al. 2007, *MNRAS*, in press
- Hu, E. M., Cowie, L. L., & McMahan, R. G. 1998, *ApJ*, 502, L99
- Hu, E. M., Cowie, L. L., Capak, P., McMahan, R. G., Hayashino, T., & Komiyama, Y. 2004, *AJ*, 127, 563
- Kalberla, P. M. W., Burton, W. B., Hartmann, D., Arnal, E. M., Bajaja, E., Morras, R., Pöppel, W. G. L. 2005, *A&A*, 440, 775
- Klein, R. I., & Castor, J. I. 1978, *ApJ*, 220, 902
- Kudritzki, R.-P., et al. 2000, *ApJ*, 536, 19
- Kunth, D., Mas-Hesse, J. M., Terlevich, E., Terlevich, R., Lequeux, J., & Fall, S. M. 1998, *A&A*, 334, 11
- Kunth, D., Leitherer, C., Mas-Hesse, J. M., Östlin, G., & Petrosian, A. 2003, *ApJ*, 597, 263
- Laursen, P., & Sommer-Larsen, J. 2007, *ApJ*, 657, L69
- Leitherer, C., et al. 1999, *ApJS*, 123, 3
- Maiz-Apellaniz, J., Mas-Hesse, J. M., Munoz-Tunon, C., Vilchez, J. M., & Castaneda, H. O. 1998, *A&A*, 329, 409
- Maíz-Apellániz, J., Pérez, E., & Mas-Hesse, J. M. 2004, *AJ*, 128, 1196
- Malhotra, S., & Rhoads, J. E. 2002, *ApJ*, 565, L71
- Malhotra, S., & Rhoads, J. E. 2004, *ApJ*, 617, L5
- Mas-Hesse, J. M., & Kunth, D. 1999, *A&A*, 349, 765
- Mas-Hesse, J. M., Kunth, D., Tenorio-Tagle, G., Leitherer, C., Terlevich, R. J., & Terlevich, E. 2003, *ApJ*, 598, 858
- Meurer, G. R., Heckman, T. M., Leitherer, C., Kinney, A., Robert, C., & Garnett, D. R. 1995, *AJ*, 110, 2665
- Murayama, T., et al. 2007, *ArXiv Astrophysics e-prints*, arXiv:astro-ph/0702458
- Nagao, T., et al. 2007, *ArXiv Astrophysics e-prints*, arXiv:astro-ph/0702377
- Neufeld, D. A. 1990, *ApJ*, 350, 216
- Osterbrock, D. E. 1989, Research supported by the University of California, John Simon Guggenheim Memorial Foundation, University of Minnesota, et al. Mill Valley, CA, University Science Books, 1989, 422 p.,
- Ouchi, M., et al. 2005, *ApJ*, 620, L1
- Prevot, M. L., Lequeux, J., Prevot, L., Maurice, E., & Rocca-Volmerange, B. 1984, *A&A*, 132, 389
- Puget, J. L., & Leger, A. 1989, *ARA&A*, 27, 161
- Valls-Gabaud, D. 1993, *ApJ*, 419, 7
- Vázquez, G. A., & Leitherer, C. 2005, *ApJ*, 621, 695
- Venemans, B. P., et al. 2002, *ApJ*, 569, L11
- Verhamme, A., Schaerer, D., & Maselli, A. 2006, *A&A*, 460, 397
- Wiklind, T., Dickinson, M., Ferguson, H. C., Giavalisco, M., Mobasher, B., Grogin, N. A., & Panagia, N. 2008, *ApJ*, 676, 781

This 2-column preprint was prepared with the AAS L^AT_EX macros v5.2.